beamlines

A helium mini-cryostat for the nanoprobe beamline ID16B at ESRF: characteristics and performance

Ricardo G. Steinmann,[a]‡ Gema Martinez-Criado,[a]§ Damien Salomon,[a] Hugo Vitoux,[a] Remi Tucoulou,[a] Julie Villanova,[a] Sylvain Laboure,[a] Joel Eymery[b] and Jaime Segura-Ruiz[a]*

[a]ESRF – The European Synchrotron, 71 Avenue des Martyrs, 30843 Grenoble, France, and [b]Univ. Grenoble Alpes, CEA, IRIG, MEM, NRS, 38000 Grenoble, France. *Correspondence e-mail: jaime.segura@esrf.fr

A helium mini-cryostat has been developed for the hard X-ray nanoprobe ID16B of the European Synchrotron to collect X-ray excited optical luminescence and X-ray fluorescence at low temperature (<10 K). The mini-cryostat has been specifically designed to fit within the strong space restrictions and high-demanding mechanical constraints imposed by the beamline to provide vibration-free operation and maximal thermal stability. This paper reports the detailed design, architecture and technical requirements of the mini-cryostat, and presents the first experimental data measured using the cryogenic equipment. The resulting cryo-system features ultimate thermal stability, fast cool-down and ultra-low vibrations. The simultaneous X-ray fluorescence and X-ray excited optical luminescence data acquired from bulk GaN and core/shell InGaN/GaN multi-quantum wells validated the excellent performance of the cryostat with ultimate resolution, stability and sensitivity.

1. Introduction

The ID16B beamline at the European Synchrotron (ESRF) provides a hard X-ray nanoprobe with a focused (50 nm × 50 nm) and intense (up to 10^{13} photons s^{-1}) beam over the 5–33 keV energy range (Martínez-Criado et al., 2016). Several characterization techniques are available: X-ray fluorescence (XRF), X-ray diffraction, X-ray absorption spectroscopy (XAS), X-ray excited optical luminescence (XEOL) and 3D phase-contrast imaging, among others. ID16B is an in-air station, which has been designed to perform in situ nano-analysis (e.g. under heating, cooling and deformation). Several sample environments have therefore been developed and used on ID16B such as a micro-heater (Villanova et al., 2017), a tensile mechanical device (Kumar et al., 2019) and a cell for operando Li ion battery studies (Vanpeene et al., 2019). To expand these in situ capabilities, an He continuous-flow-type cryostat was the instrument of choice for low-temperature acquisitions ($T < 10$ K). The cryo-system provides several advantages, including sample preservation from beam-induced radiation damage (George et al., 2012; Wallander & Wallentin, 2017), reduction of thermal motions of atoms (relevant for XAS), and specifically much more intense and narrower spectral lines for XEOL than those taken at room temperature (RT) (Martínez-Criado et al., 2007). Thus, for the latter there is a significant reduction in the total exposure time required to obtain a good signal-to-noise ratio, as well as a superior discrimination among different radiative recombi-nation channels (Yu & Cardona, 2010). Commercially available cryo-systems allowing nanometre resolution cannot answer to the specific needs and constraints imposed by the
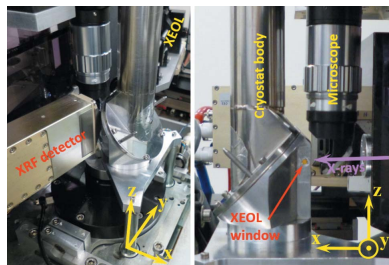
experimental setup of ID16B. Therefore, the implementation of a specific solution is required.

In this work, we present the main characteristics of the helium continuous-flow mini-cryostat specifically designed for the ID16B nanoprobe, which enables long-term investigations of samples at low temperature (LT) over several days. The cryo-system allows simultaneous measurements of XEOL and XRF in the temperature range between 3 K and 50 K. A series of tests have been performed to assess the impact of the integration of the cryostat on the X-ray nanoprobe stability and spatial resolution. Finally, concurrent XEOL and XRF mappings of single nanowires are shown to demonstrate the reliability and excellent performance of the He mini-cryostat in terms of both thermal stability and spatial stability.

2. Design and main characteristics

The experimental setup of ID16B imposes strong XYZ space constraints to its sample environments (see Fig. 1). In the X direction (along the beam) the sample must be positioned in the focal plane of the X-ray optics, located only ~4 cm away from the focusing device housing and a few millimetres from the optical microscope assembly used for sample visualization. In the Y direction, the XRF detector and XEOL collection optics limit the space for the mini-cryostat because both must be placed sideways and as close as possible to the sample. In the Z direction, the optical microscope limits the upper positioning of the mini-cryostat. Therefore, there are severe constraints for motion and a suitable sample positioning and alignment. Thus, to address these limitations the mini-cryostat has been designed with a cylindrically shaped vertical housing, as shown in Fig. 1.

In order to reduce the size of the mini-cryostat, we decided to keep the sample fixed. Consequently, it is mounted on the beamline set of XYZ translation stages for both precise positioning and scanning of the sample. The XRF and XEOL images are obtained by raster scanning the mini-cryostat with respect to the X-ray nanobeam and measuring the spectral distribution of the XRF and XEOL signals coming from the sample for each point.

The technology behind the mini-cryostat is an He gas stream flowing through a closed circuit with vacuum isolation. The sample is cooled by an aluminium sample holder firmly anchored to this circuit. The He gas at a temperature below 4 K enters the mini-cryostat by means of an Oxford low-loss transfer tube and flows through the cooling circuit. The helium circuit consists of two heat exchangers, as shown in Fig. 2(a): the first main exchanger cools the sample holder, whereas the
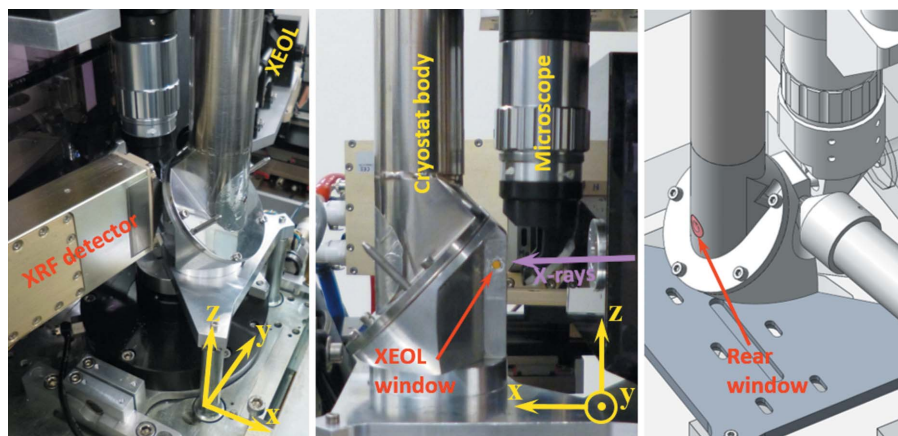

Figure 1
Beamline XYZ sample stage with the mini-cryostat in place. The left-hand picture shows the XRF detector on the left and the XEOL optical collection on the right, just behind the cryostat. The central picture shows a lateral view with the sapphire window for the XEOL and the optical microscope in place. The schematic drawing shows the position of the XEOL optical collection during the measurements.
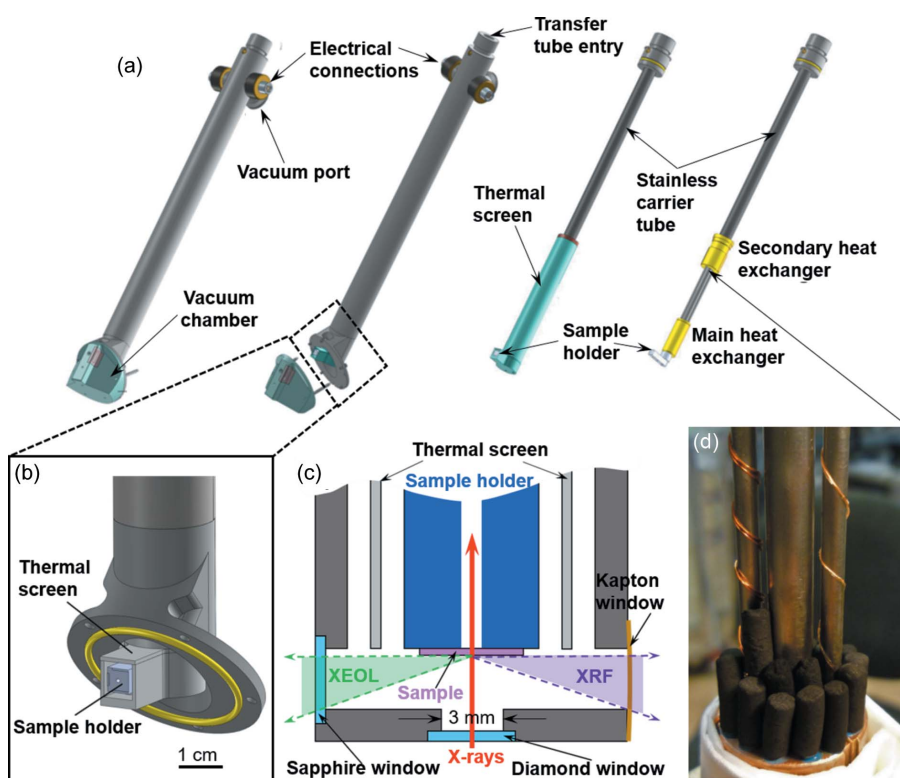

Figure 2
(a) Main parts of the He mini-cryostat body. (b) Details of the sample holder. (c) Top-view cut schematics of the He mini-cryostat showing the main components at the sample position. (d) Activated charcoal pellets.

second uses part of the remaining enthalpy of the helium to cool the thermal screen (for detailed information on the working cycle see http://as-specialdevices.com/index.php/fr/news-and-announcements). Both exchangers are coated with a gold layer (5 µm thick) to minimize radiation heat. The vacuum chamber is composed of two parts, one fixed and the other removable, as shown in Fig. 2(a). The removable part holds the windows, a sealing ring and two pin guides ensure a quick and safe positioning.

The sample holder, shown in Fig. 2(b), is mounted on the main heat exchanger and fixed by a specially shaped brass screw. It is made of ultra-high purity aluminium in order to avoid parasitic peaks within the XRF spectra. The sample holder can accommodate standard Si_3N_4 membranes with a frame size 5 mm × 5 mm. However, owing to the limited size of the frontal diamond window frame, only a 3 mm-diameter disk is accessible to the X-ray beam.

As shown in Fig. 1, both XRF and XEOL detection systems are located in the horizontal plane pointing to the sample with an angle of approximately 10°. A top-view cut of the He mini-cryostat drawing is shown in Fig. 2(c). At the front side, a thin polycrystalline diamond window (5 mm diameter and 300 µm thick) lets both the X-ray incoming beam and the visible light from the optical microscope enter the mini-cryostat. Samples can be probed with the X-ray nanofocused beam, and visualized at the same time with the optical microscope working with back-scattered light. At the XRF collection side, a Kapton rectangular window (25 µm thick) is used in order to minimize XRF absorption. The XEOL signal, on the other hand, is detected through a high-quality sapphire window (5 mm diameter and 300 µm thick). This window features extreme surface hardness resistance and large wavelength transmission ranging from UV to mid-infrared with negligible parasitic luminescence. Finally, a 3 mm-diameter, 25 µm-thick Kapton rear window allows the transmitted beam to be passed through a hole in the sample holder to collect measurements in transmission mode.

The compatibility with nanoscale resolution measurements requires the reduction or elimination whenever possible of vibrations and thermal drifts of the sample. Under operation conditions, the use of vacuum pumps is avoided and only static vacuum is allowed for this instrument. A sorption pump made of a few grams of activated charcoal pellets bonded on the bottom surface of the secondary heat exchanger [Fig. 2(d)] is used. At LT, the adsorption capacity of the activated charcoal reaches several times the volume of the cryostat, allowing the adsorption of gas coming from degassing of the inner surfaces of the mini-cryostat and the air permeability of the Kapton windows. The static vacuum can thus be preserved for up to three days within the cryostat.

Boiling of cryogenic liquid, cavitation, pressure drop or inhomogeneous helium flow can be major sources of vibrations and must be avoided. Therefore, the mini-cryostat operates under a continuous and very low flow of helium gas. Moreover, low-frequency thermal drifts of the cryo-system can also induce a noticeable sample shift. Typically, the expansion coefficient of the materials used in the fabrication

of the mini-cryostat (copper, aluminium, stainless steel) is of the order of 10^{-5} K^{-1}. This means that, to limit the thermal drift of the sample below 50 nm, the temperature stability at the sample position must be $\Delta T/T < 0.01$. In order to attain this level of regulation, sample and thermal screen temperatures are controlled independently, maintaining a fixed gradient between them and the room temperature. In order to regulate the temperature, the main heat exchanger is equipped with a cartridge resistor of 50 Ω (25 W) and a calibrated Cernox thermometer that is fixed to the bottom of the sample holder. In the secondary heat exchanger, a wound-wire heater (Steinmann & Vitoux, 2015) and a silicon thermometer are used for this purpose. A dual-channel temperature controller connected to these heaters and sensors regulates the sample and screen temperatures. The mini-cryostat is equipped with two electrical connectors. One serves to connect the temperature sensors and heaters to the dual-channel controller. The second is connected to eight cables (copper and manganin) arriving at the sample holder, which in the near future will be used to perform electrical measurements. The weight of the entire mini-cryostat is 490 g without the transfer tube. In short, the cryo-system includes all the necessary components needed for the mini-cryostat operation such as the transfer line, dual channel temperature controller, pumping system, pressure gauge and all the necessary vacuum fittings.

3. Operation and performance

Before cooling, the mini-cryostat must be pumped with a turbo-molecular pump and the secondary heater must be warmed up to 320 K in order to desorb the activated charcoals. Once the vacuum reaches a pressure lower than 5 × 10^{-6} mbar, the vacuum port is sealed using a gate valve and then the pumping system is stopped. Thanks to the relatively small dimensions of the mini-cryostat, sample and thermal screen the cooling process takes only a few minutes, as seen in Fig. 3(a). Once the temperatures of the two heat exchangers are stabilized ($\Delta T/T < 10^{-2}$), the thermal expansion-related drift of the sample should be less than 50 nm. The temperature stabilizes around 30 min after the He gas stream has started flowing through the close circuit [Fig. 3(b)], and remains stable for several hours [Figs. 3(c) and 3(d)]. The sample fixation is of paramount importance, as it should provide excellent thermal conductivity, mechanical stability at LT and negligible parasitic XRF signal. Using vacuum grease instead of the more common Ag or Au varnish allows us to avoid contamination of the XRF spectra. A thin layer of UHV vacuum grease (as Apiezon N) allows a very good thermal and mechanical anchoring of the sample. A differential measurement of the temperature between the sample and its holder (by replacing the sample with an identical thermometer of that of the sample holder) showed a $\Delta T < 0.03$ K at 3 K and negligible at higher temperatures.

The autonomy of the cryostat strongly depends on the working temperature of the secondary heat exchanger. For instance, at 20 K the cryostat can operate for at least 3 days,
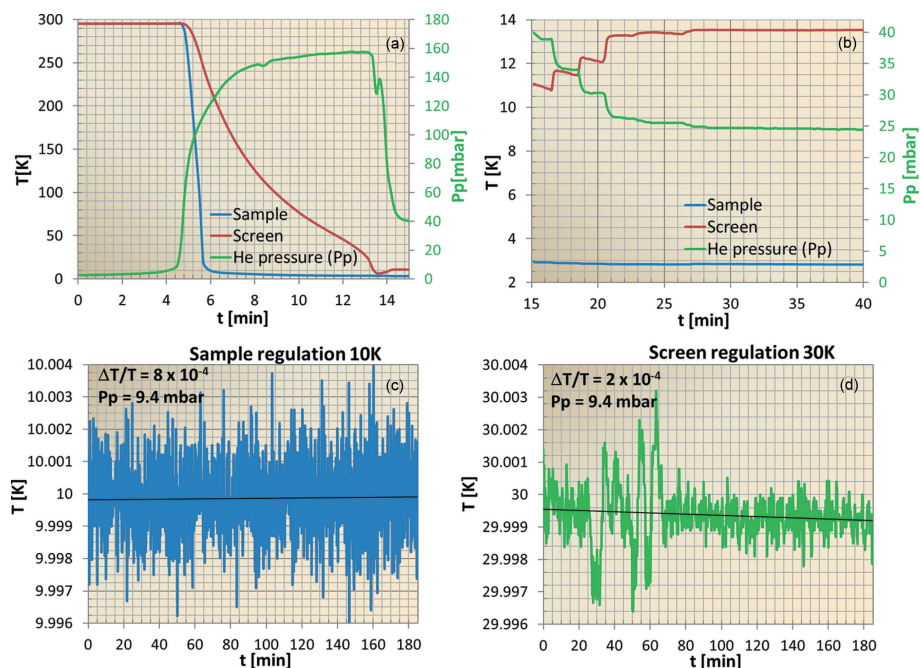
Figure 3
Sample and thermal screen temperature (left axes) and He pumping pressure (right axes) during (*a*) the initial cooling and (*b*) the lowest temperatures of the cryostat without regulation. Temperature regulation at (*c*) 10 K for the sample (blue) and (*d*) 30 K for the thermal screen (green).

The XEOL spectra of a bulk GaN crystal (Martínez-Criado *et al.*, 2001) at RT and 8 K are shown in Fig. 5. They were recorded using an Ocean Optics Maya 2000 Pro spectrometer, providing a spectral resolution of about 12 meV at 3.5 eV. The specifications of the XEOL setup are described elsewhere (Martínez-Criado *et al.*, 2012, 2014). As expected, the intensity of the near-band-edge emission at LT is several orders of magnitude higher, with much narrower peaks at LT than at RT. The narrowing of the luminescence lines allows the neutral donor (I2) and acceptor (I1) bound excitons, and donor–acceptor pair (DAP) transitions of the GaN, as well as several discrete phonon sidebands to be resolved and identified (Reshchikov & Morkoç, 2005). The measured energy separation of about 90 meV between the sidebands is in good agreement with the A_1 (LO) phonon energy reported for GaN at LT (Davydov *et al.*, 1998; Song *et al.*, 2006).

whereas at 35 K the sorption pump will saturate after 2 days. Sample change requires warming the cryo-system up using the heaters to improve the degassing of the sorption pump and typically takes 2 h.

In order to evaluate the stability of the mini-cryostat, a specific test object (Tungsten cross with 30 nm-wide lines deposited on a silicon substrate) was characterized by nano-XRF. The measurements were performed first at RT without the mini-cryostat, and then at 8 K with the sample inside the mini-cryostat. Horizontal and vertical lines were scanned across the focused X-ray nanobeam while the $L\alpha$ XRF line of W was measured. Plots of the tungsten line profiles acquired at RT and LT are shown in Fig. 4. The profiles taken with or without the mini-cryostat do not show any significant difference either in the full width at half-maximum (FWHM) or in the shape of the measured Gaussian curves within our experimental accuracy. These results clearly show that the level of vibration induced by the mini-cryostat does not noticeably modify the XRF acquisitions, highlighting its excellent spatial stability.

4. XEOL measurements

Among the techniques available on ID16B, XEOL is one that can benefit the most from low temperatures. Cooling can efficiently decrease non-radiative recombination processes, enhancing the XEOL intensity, while narrowing the XEOL emission peaks owing to the reduction of homogeneous broadening (Yu & Cardona, 2010). Thus, low temperatures can notably lower the accumulation time while increasing the resolving power of the spectral lines contributing to the total XEOL signal.

To further examine the capabilities offered by the He mini-cryostat, a specific area of a core/shell InGaN/GaN multi-quantum wells (MQWs) wire has been studied by combining XRF and XEOL acquisitions at LT. Details of the growth process and characteristics of the wire can be found elsewhere (Koester *et al.*, 2011). For this study, several wires from the same sample were dispersed onto an Si_3N_4 membrane and cooled down to 6 K using the mini-cryostat.
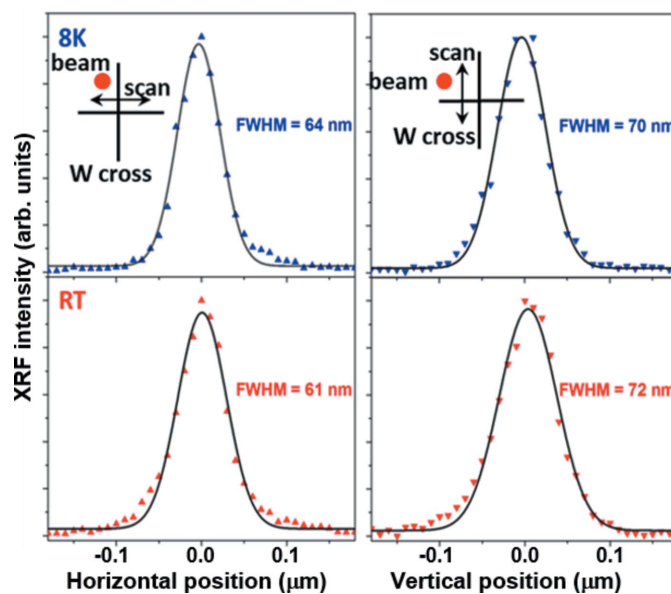
Figure 4
Tungsten $L\alpha$ XRF intensity profiles acquired across narrow W lines measured at 8 K (top) and RT (bottom).
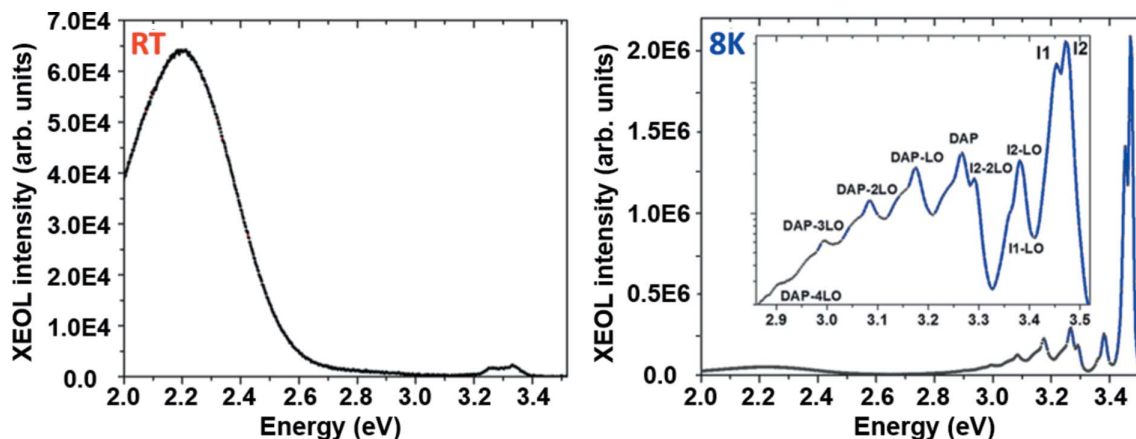
Figure 5
XEOL spectra of bulk GaN taken at RT and 8 K. The inset shows details of the near-band-edge emission in logarithmic scale.

Fig. 6(*a*) shows a scanning electron microscope (SEM) image of a complex core/shell InGaN/GaN MQWs wire. Charging effects caused by the poor electrical conductivity of the substrate are behind the low quality and magnification of the SEM image. However, we observed that the wire has an irregular morphology, different from perfect hexagonal wires with flat surfaces, which are often observed for such material and growth technique (Song *et al.*, 2006). This irregular shape is caused by specific growth conditions which promote the appearance of different polarity domains (Salomon *et al.*, 2017), and by the coalescence of two objects of different heights. XEOL and XRF maps were acquired with a pixel size of 70 nm × 70 nm and an accumulation time of 500 ms per pixel, for a total acquisition time of about 1.5 h.
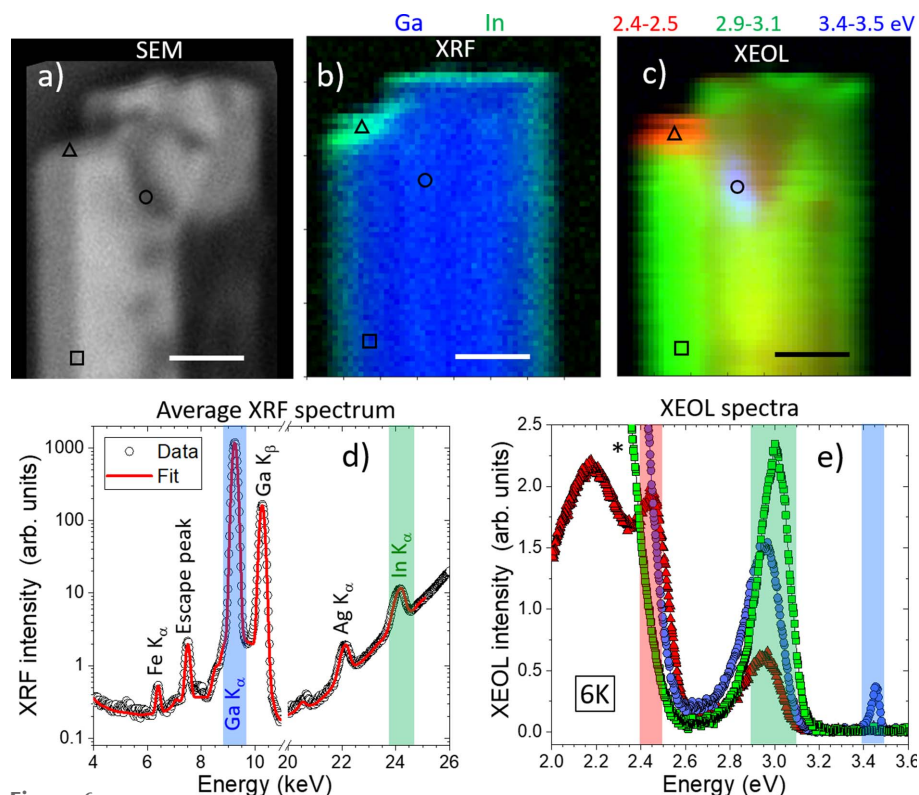
Fig. 6(*b*) shows the superimposed XRF intensity maps of Ga (blue) and In (green) *K*α lines. Top and lateral walls of the core-shell wire display high In *K*α intensity regions owing to the QWs in the wire shell. Another region, observed as a terrace by SEM and marked with a triangle, exhibits a very high In *K*α intensity. The average XRF spectrum in Fig. 6(*d*) shows the presence of some residual elements such as Fe and Ag. The spatial distribution of these elements (not shown) suggests Fe is in the wire, whereas Ag is in the substrate. Finally, Fig. 6(*c*) shows the superimposed XEOL intensity maps for three energy ranges: 2.4–2.5 eV (red); 2.9–3.1 eV (green); 3.4–3.5 eV (blue). In contrast to the XRF map, most of the morphological irregularities observed by SEM correlate well with the features spotted in the XEOL map. Various regions of the wire exhibit different optical properties revealed by XEOL. In the 2.4–2.5 eV energy region (red map), the XEOL intensity corresponds well with the position of the terrace, having a higher In content according to the XRF map. Both the red-shifted XEOL emission and the In *K*α XRF intensity suggest that the InGaN wells have a higher In concentration. Similarly, the XEOL intensity in the energy

Figure 6
(*a*) SEM image of an irregular core/shell InGaN/GaN MQWs wire characterized simultaneously by XRF and XEOL at 6 K. (*b*) Superimposed XRF intensity maps of Ga (blue) and In (green) *K*α-lines. (*c*) Superimposed XEOL intensity maps for three energy ranges: 2.4–2.5 eV (red); 2.9–3.1 eV (green); 3.4–3.5 eV (blue). (*d*) Average XRF spectrum of the wire. (*e*) XEOL spectra acquired in an area of 140 nm × 140 nm (2 × 2 pixels) in three different positions as indicated by the symbols (triangle, square and circle) in the images. The asterisk shows the common GaN yellow defect band. The coloured energy ranges illustrate those plotted in the superimposed maps. Scale bars correspond to 1 μm.

range 3.4–3.5 eV (corresponding to the near-edge emission of GaN at LT) shows a spatially localized GaN emission. This band most likely comes from a region where the GaN core was not covered by the MQWs, as inferred from the SEM image.

In order to better identify the optical characteristics of the various regions of the wire, Fig. 6(e) shows the XEOL spectra acquired in three different locations (2 × 2 pixels, 140 nm × 140 nm) as indicated by the symbols (triangle, square and circle) in the images. The XEOL spectrum taken from the terrace exhibits a red-shifted emission that is different from the well known yellow band of GaN (marked with an asterisk), usually assigned to either gallium vacancy-related defects (Saarinen *et al.*, 1997) or carbon-related defects (Zhang & Kuech, 1998). This finding corroborates the existence of In-richer InGaN wells in this region (Kapoor *et al.*, 2020). The XEOL spectrum acquired in the central portion shows the near-edge emission of GaN, as well as the dominant violet band around 3.0 eV attributed to the transitions from the InGaN/GaN MQWs. Finally, the XEOL spectrum collected at the homogeneous lateral wall of the wire displays a single and intense peak centred around 3.0 eV, coming from the InGaN/GaN MQWs. In summary, our XRF/XEOL acquisitions in 2D demonstrate the high thermal stability, superior spectral sensitivity and ultimate spatial resolution achieved during long acquisitions (1.5 h for the maps in Fig. 6) using the He mini-cryostat.

5. Conclusions

A helium continuous-flow mini-cryostat has been implemented for low-temperature X-ray nanoanalysis at the ID16B beamline of ESRF. The device was designed to perform simultaneous collection of XRF and XEOL data in the temperature range between 3 K and 50 K, and to meet the highly demanding requirements imposed by the hard X-ray nanoprobe setup. The resulting cryo-system showed high spatial and temperature stability at temperatures as low as 6 K. Efficient XRF and XEOL signal detection was demonstrated with an outstanding lateral spatial resolution limited by the spot size. The performance of the mini-cryostat has been demonstrated through examination of core/shell InGaN/GaN MQWs wires with irregular geometrical morphology. Owing to the intense XEOL signal at LT, several emissions were identified and spatially localized within the wire. The XEOL lines correlated well with nanometre-sized irregularities observed in the wire, corroborating the stability and good resolution achieved by the mini-cryostat under real measurement conditions. Aside from the improvement in the XEOL capability, this new instrument can greatly reduce the potential radiation damage suffered by sensitive samples with the new ESRF extremely brilliant source.

References

Davydov, V. Y., Kitaev, Y. E., Goncharuk, I. N., Smirnov, A. N., Graul, J., Semchinova, O., Uffmann, D., Smirnov, M. B., Mirgorodsky, A. P. & Evarestov, R. A. (1998). *Phys. Rev. B*, **58**, 12899–12907.

George, G. N., Pickering, I. J., Pushie, M. J., Nienaber, K., Hackett, M. J., Ascone, I., Hedman, B., Hodgson, K. O., Aitken, J. B., Levina, A., Glover, C. & Lay, P. A. (2012). *J. Synchrotron Rad.* **19**, 875–886.

Kapoor, A., Finot, S., Grenier, V., Robin, E., Bougerol, C., Bleuse, J., Jacopin, G., Eymery, J. & Durand, C. (2020). *Appl. Mater. Interfaces*, **12**, 19092–19101.

Koester, R., Hwang, J., Salomon, D., Chen, X., Bougerol, C., Barnes, J. P., Le Si Dang, D., Rigutti, L., de Luna Bugallo, A., Jacopin, G., Tchernycheva, M., Durand, C. & Eymery, J. (2011). *Nano Lett.* **11**, 4839–4845.

Kumar, R., Villanova, J., Lhuissier, P. & Salvo, L. (2019). *Acta Mater.* **166**, 18–27.

Martínez-Criado, G., Alén, B., Sans, J. A., Homs, A., Kieffer, I., Tucoulou, R., Cloetens, P., Segura-Ruiz, J., Susini, J., Yoo, J. & Yi, G. (2012). *Nucl. Instrum. Methods Phys. Res. B*, **284**, 36–39.

Martínez-Criado, G., Miskys, C. R., Cros, A., Ambacher, O., Cantarero, A. & Stutzmann, M. (2001). *J. Appl. Phys.* **90**, 5627–5631.

Martínez-Criado, G., Segura-Ruiz, J., Alén, B., Eymery, J., Rogalev, A., Tucoulou, R. & Homs, A. (2014). *Adv. Mater.* **26**, 7873–7879.

Martínez-Criado, G., Steinmann, R. G., Alén, B., Labrador, A., Fuster, D., Ripalda, J. M., Homs, A., Labouré, S. & Susini, J. (2007). *Rev. Sci. Instrum.* **78**, 025106.

Martínez-Criado, G., Villanova, J., Tucoulou, R., Salomon, D., Suuronen, J.-P., Labouré, S., Guilloud, C., Valls, V., Barrett, R., Gagliardini, E., Dabin, Y., Baker, R., Bohic, S., Cohen, C. & Morse, J. (2016). *J. Synchrotron Rad.* **23**, 344–352.

Reshchikov, M. A. & Morkoç, H. (2005). *J. Appl. Phys.* **97**, 061301.

Saarinen, K., Laine, T., Kuisma, S., Nissilä, J., Hautojärvi, P., Dobrzynski, L., Baranowski, J. M., Pakula, K., Stepniewski, R., Wojdak, M., Wysmolek, A., Suski, T., Leszczynski, M., Grzegory, I. & Porowski, S. (1997). *Phys. Rev. Lett.* **79**, 3030–3033.

Salomon, D., Messanvi, A., Eymery, J. & Martínez-Criado, G. (2017). *Nano Lett.* **17**, 946–952.

Song, D. Y., Basavaraj, M., Nikishin, S. A., Holtz, M., Soukhoveev, V., Usikov, A. & Dmitriev, V. (2006). *J. Appl. Phys.* **100**, 113504.

Steinmann, R. G. & Vitoux, H. (2015). *Rev. Sci. Instrum.* **86**, 016107.

Vanpeene, V., Villanova, J., King, A., Lestriez, B., Maire, E. & Roué, L. (2019). *Adv. Energy Mater.* **9**, 1803947.

Villanova, J., Daudin, R., Lhuissier, P., Jauffrès, D., Lou, S., Martin, C., Labouré, S., Tucoulou, R., Martínez-Criado, G. & Salvo, L. (2017). *Mater. Today*, **20**, 354–359.

Wallander, H. & Wallentin, J. (2017). *J. Synchrotron Rad.* **24**, 925–933.

Yu, P. Y. & Cardona, M. (2010). *Fundamentals of Semiconductors: Physics and Materials Properties*, 4th ed. Berlin: Springer-Verlag.

Zhang, R. & Kuech, T. F. (1998). *Appl. Phys. Lett.* **72**, 1611–1613.